Bismuth Sulfide Nanorods as a Precision Nanomedicine for *in Vivo* Multimodal Imaging-Guided Photothermal Therapy of Tumor

Jing Liu,[†,§] Xiaopeng Zheng,[†,‡,§] Liang Yan,[†] Liangjun Zhou,[†,‡] Gan Tian,[†] Wenyan Yin,[†] Liming Wang,[†] Ying Liu,[†] Zhongbo Hu,[‡] Zhanjun Gu,[*,†] Chunying Chen,[*,†] and Yuliang Zhao[*,†]

[†]CAS Key Laboratory for Biomedical Effects of Nanomaterials and Nanosafety, National Center for Nanoscience and Technology of China, and Institute of High Energy Physics, Chinese Academy of Sciences, Beijing, China and [‡]College of Materials Science and Optoelectronic Technology, University of Chinese Academy of Sciences, Beijing, China. [§]These authors contributed equally.

ABSTRACT Here, we present a precision cancer nanomedicine based on Bi_2S_3 nanorods (NRs) designed specifically for multispectral optoacoustic tomography (MSOT)/X-ray computed tomography (CT)-guided photothermal therapy (PTT). The as-prepared Bi_2S_3 NRs possess ideal photothermal effect and contrast enhancement in MSOT/CT bimodal imaging. These features make them simultaneously act as "satellite" and "precision targeted weapon" for the visual guide to destruction of tumors *in vivo*, realizing effective tumor destruction and metastasis inhibition after intravenous injection. In addition, toxicity screening confirms that Bi_2S_3 NRs have well biocompatibility. This triple-modality-nanoparticle approach enables simultaneously precise cancer therapy and therapeutic monitoring.

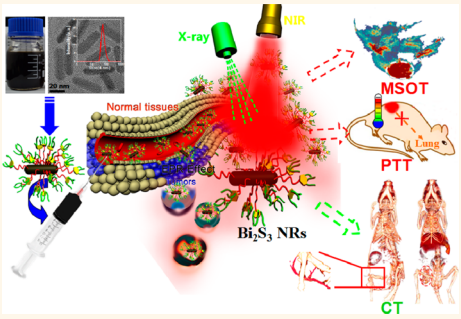

KEYWORDS: Bi_2S_3 nanorods · thin bandgap semiconductor · multispectral optoacoustic tomography · X-ray computed tomography · photothermal therapy

Nanomedicines offer unprecedented opportunities to reach the objectives such as promoting the precision treatment of cancer and mitigating undesired side effects.[1,2] Over the past decade, precision nanomedicines have been extensively explored to fabricate theranostics that integrate multiple imaging approaches and therapeutic modalities.[3−13] Among these investigations, imaging-guided photothermal therapy (PTT) has drawn considerable attention. PTT employs an efficient light harvesting agent for the localized conversion of the tissue-transparent near-infrared (NIR, λ = 700−1100 nm) light into heat to ablate cancer cells.[14−20] Multimodality imaging provides PTT with real-time guidance to diagnose disease, guide procedures, monitor therapeutic response, and treat disease with greater specificity and sensitivity.[21−32] By distinguishing from the assorted imaging approaches, X-ray computed tomography (CT) is a mainstay of clinical diagnostic modality with the advantages of high resolution, no depth limitation, and allowing for three-dimensional (3D) reconstruction.[33−35] However, pharmacokinetic limitations of clinically available CT contrast agents (small iodinated molecules), including short circulation half-lives and nonspecific distribution, are the main causes of CT failure for tumor target imaging and angiography.[36,37] Moreover, various intrinsic limitations of CT imaging particularly with respect to poor soft tissue contrast, low throughput capacity, limited accessibility, and ionizing radiation also represent as notable hurdles that prevent the application of CT for clinical diagnosis.[38] Thus, combining CT with another imaging technique that can fully take the advantages of each while avoiding the drawbacks of both is more preferable for the precision diagnosis since no single modality is perfect and sufficient to obtain all the necessary information.[39] From this point, multispectral optoacoustic tomography (MSOT)

* Address correspondence to zjgu@ihep.ac.cn, chenchy@nanoctr.cn, zhaoyuliang@ihep.ac.cn.

Received for review October 28, 2014 and accepted January 5, 2015.

Published online January 05, 2015
10.1021/nn506137n

based on the photoacoustic effect induced by NIR absorption and subsequent thermal expansion is harnessed to render much higher spatial resolution to soft tissues and offer real-time monitoring.[40−43] Therefore, the bimodal imaging associating CT with MSOT is a good choice for precision diagnosis, which could overcome the shortcomings of two imaging modalities and leverage the advantages of the both, providing the improved feasibility, precision, and efficacy of diagnosis.[44,45]

Bismuth-based nanoparticles (NPs) such as Bi_2S_3 nanodots and Bi_2Se_3 nanoplates have been employed as CT contrast agents, arising from their high X-ray attenuation capability, long residence time, low toxicity, no residues in the organism, and cost effectiveness, which thereby reduces the required dose and allows more flexibility in the clinical setting.[46−48] Moreover, as a direct thin band gap n-type semiconductor (~1.3 eV), Bi_2S_3 NPs with high NIR absorption coefficient have been used as the NIR-absorber to extend the absorption wavelength to the NIR region for the improvement of solar harnessing capability of solar cells.[49−52] Encouraged by the ideal NIR absorption property of Bi_2S_3 NPs, it is very possible to use them as the MSOT and PTT agents, which thus makes them become a simple but powerful precision nanomedicine that comprises Bi_2S_3 NPs only without any additional functional components to simultaneously achieve MSOT/CT bimodal imaging and PTT.

To realize the above speculation, we fabricated Bi_2S_3 nanorods (NRs) and then for the first time applied them as a single-phase theranostic platform that leveraged MSOT/CT bimodal imaging to enable spatial- and temporal-specifically guided PTT. The theranostic principle based on the Bi_2S_3 NRs is presented in Scheme 1. First, uniform oleic acid (OA)-coated Bi_2S_3 (OA-Bi_2S_3) NRs were scalably prepared by a readily solvothermal method. Second, an amphiphilic nontoxic surfactant Tween was applied to functionalize Bi_2S_3 NRs to render them water dispersibile and prolong the residence time *in vivo*. Next, MSOT and CT were employed to visualize the trace of Bi_2S_3 NRs against the period of circulation *in vivo*. We successfully demonstrated that the Bi_2S_3 NRs can be used not only as a powerful CT contrast agent to realize both the angiography and organic imaging, but also as the MSOT contrast enhancer to real-time monitor the presence of NRs at the tumor site. Finally, these Bi_2S_3 NRs further serve as powerful photothermal therapeutics to effectively ablate primary tumors and preclude their metastasis. The strategy provides a simple but powerful theranostic platform to achieve multimodality imaging-guided PTT for precision cancer treatment.

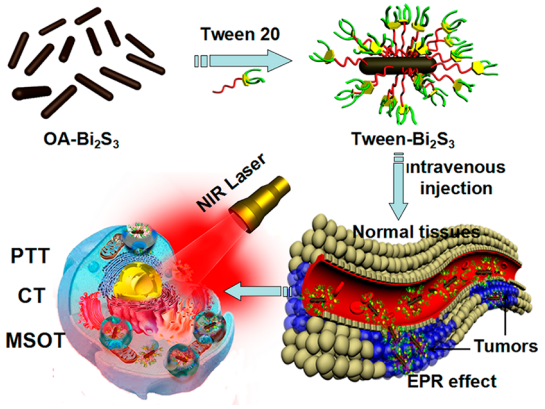

Scheme 1. Schematic illustration of the theranostic principle based on the unique properties of the Bi_2S_3 NRs.

RESULTS AND DISCUSSION

Typical transmission electron microscope (TEM) images of the as-synthesized Bi_2S_3 NRs showed a uniform size with diameter of about 10 nm and length up to 50 nm (Figure 1a; Figure S1, Supporting Information). X-ray diffraction (XRD), energy dispersive X-ray spectroscopy (EDS), and X-ray photoelectron spectroscopy (XPS) were conducted to investigate the chemical composition and purity of the as-prepared Bi_2S_3 NRs. The XRD pattern shown in Figure S3, panel a demonstrates that all the peaks could be well indexed to the orthorhombic Bi_2S_3 crystal (JCPDS No. 43−1471). EDS results further confirmed that only Bi and S were detected in the sample, except the C and O that came from the surface modification and environment (Figure S3b). To further evaluate the NRs composition and oxidation state, XPS characterization was performed. Two peaks centered at 159.9 and 163.8 eV, as shown in Figure S3, panel c, correspond to the Bi $4f_{7/2}$ and Bi $4f_{5/2}$ peaks of Bi^{3+} ions, respectively. The peak located at 161.2 eV is assigned to S^{2+} 2p.[37] No peaks were detected for metallic Bi and other impurities, which indicates the high purity of the as-prepared Bi_2S_3 NRs. To render them well dispersibility in physiological solutions and improve their biocompatibility, the as-prepared Bi_2S_3 NRs were further functionalized with a commercially available surfactant Tween 20. Tween could enable them with good dispersibility in water while protecting the NRs from nonspecific adsorption of proteins due to their unique molecular structure, which thus offers an opportunity for NRs to home in tumor *via* enhanced permeation and retention (EPR) effect.[2,3] After Tween surface modification, the hydrodynamic size of Bi_2S_3 NRs as illustrated in inset of Figure 1, panel a is about 90 nm, that is, larger than that of NRs in the TEM image (50 nm), which confirms that a condense Tween layer cover on the surface of the NRs is present. The successful functionalization of OA-Bi_2S_3 with Tween 20 is also confirmed by the Fourier transform infrared (FTIR) spectra as shown in Figure S3, panel d. Tween-modified Bi_2S_3 (Tween-Bi_2S_3) NRs exhibited well stability in various physiological solutions (Figure S2).

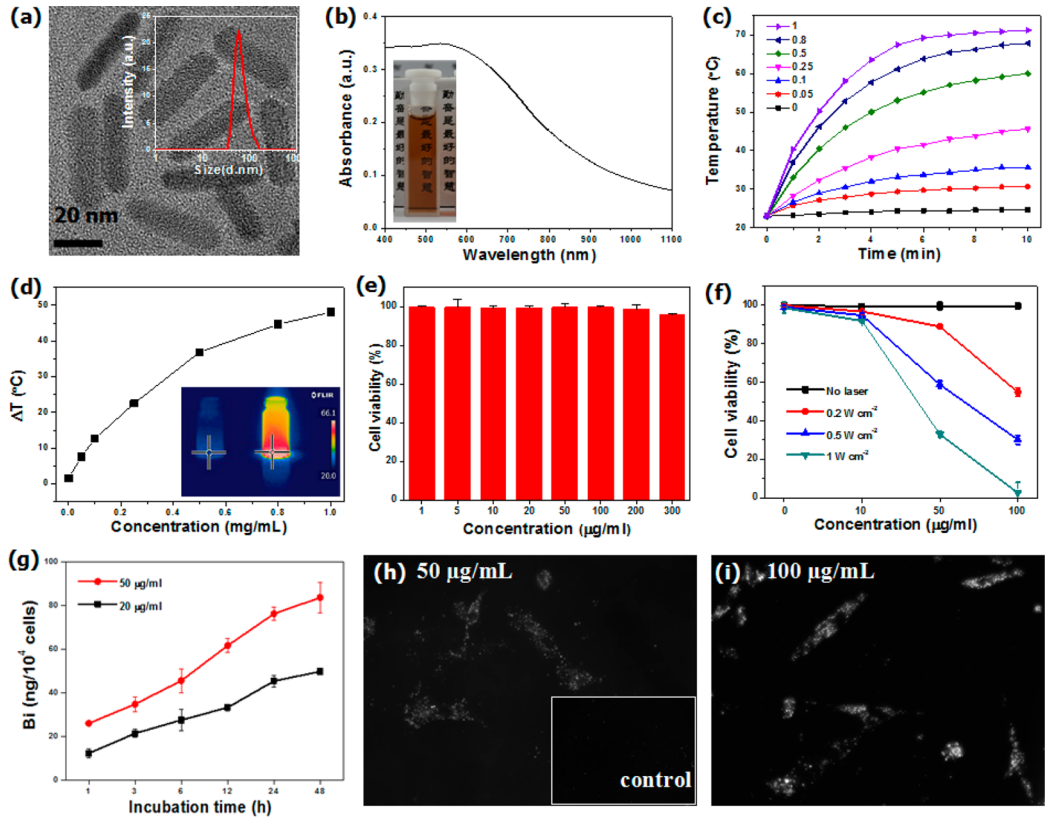

Figure 1. Bi_2S_3 NRs characterization and *in vitro* cell experiments. (a) TEM images of as-prepared Bi_2S_3 NRs. Inset: dynamic light scattering figure of Bi_2S_3 NRs. (b) UV−vis−NIR absorbance spectra of Bi_2S_3 NRs. Inset: photos of as-prepared Bi_2S_3 NRs solution in deionized (DI) water. (c) The photothermal profiles of pure water and aqueous dispersions of Bi_2S_3 NRs with different concentrations under 808 nm laser irradiation with a power density of 1 W cm^{-2}. (d) Plot of temperature change (ΔT) of Bi_2S_3 NRs solution of different concentrations over a period of 10 min. Inset: IR images of water and Bi_2S_3 NRs solution (1 mg mL^{-1}, 1 mL) after laser irradiation (1 W cm^{-2}, 10 min). (e) Cell viability of 4T1 cells after cultured with various concentrations of Bi_2S_3 NRs for 24 h. (f) Cell viability of 4T1 cells incubated with Tween-Bi_2S_3 NRs at various concentrations upon NIR irradiation. (g) Time-dependent cellular uptake of Tween-Bi_2S_3 NRs determined by inductively coupled plasma mass spectrometry (ICP-MS) after incubation at concentrations of 20 and 50 μg mL^{-1}. (h, i) Dark-field optical microscopy image of cells incubated with different concentrations of Bi_2S_3 NRs for 24 h, while control was shown in the inset.

As shown in Figure 1, panel b, the aqueous solution of Tween-Bi_2S_3 NRs was brown, and the UV−vis-NIR spectrum exhibited that Bi_2S_3 NRs have a broad absorption in the NIR region (700−1100 nm) since it is a semiconductor with a band gap of 1.3 eV that expand the light absorption to NIR region.[49,50] The high NIR absorption capability of Bi_2S_3 NRs motivates us to investigate their NIR photothermal properties, which play a key role for their applications in MSOT and PTT. To examine their photothermal properties, the temperature trends of the aqueous dispersion of Bi_2S_3 NRs with different concentrations (0.05, 0.1, 0.25, 0.5, 0.8, and 1 mg mL^{-1}) were measured under the irradiation of 808 nm NIR laser (1 W cm^{-2}), and pure water was used as the control (Figure 1c). The temperature of Bi_2S_3 NRs samples raised rapidly accompanied with the increase of irradiation time or the concentration of the Bi_2S_3 NRs. For example, the temperature of the aqueous dispersion of the Bi_2S_3 NRs with the concentration of 1 mg mL^{-1} can increase by ~50 °C within 10 min (Figure 1d), while the temperature of pure water showed mild temperature change (only ~5 °C). These results imply that the Bi_2S_3 NRs can rapidly and efficiently convert the NIR energy into thermal energy. Moreover, according to the obtained data (Figure S4a,b), the photothermal conversion efficiency is calculated to be ~28.1% (see Supporting Information for details).[25,53] The study on photostability of Bi_2S_3 NRs was also carried out, and the results clearly show that upon the continuous irradiation by NIR laser for 1 h, the absorption of Bi_2S_3 NRs has no obvious reduction, which indicates their good photostability that is very important toward for further applications (Figure S5). Therefore, Bi_2S_3 NRs have the remarkable potential to be applied as the PTT agent and MSOT contrast agent.

For further biomedical applications, it is necessary to understand the cytotoxicity of these NRs. First, the capability to internalize a sufficient amount of NRs in cancer cells is measured since it is critical for their toxicity effect and the further therapeutic effect. Quantification of cellular internalization of Bi_2S_3 NRs reveals that with the increase of NRs concentration and incubation time, the internalization of NRs steadily

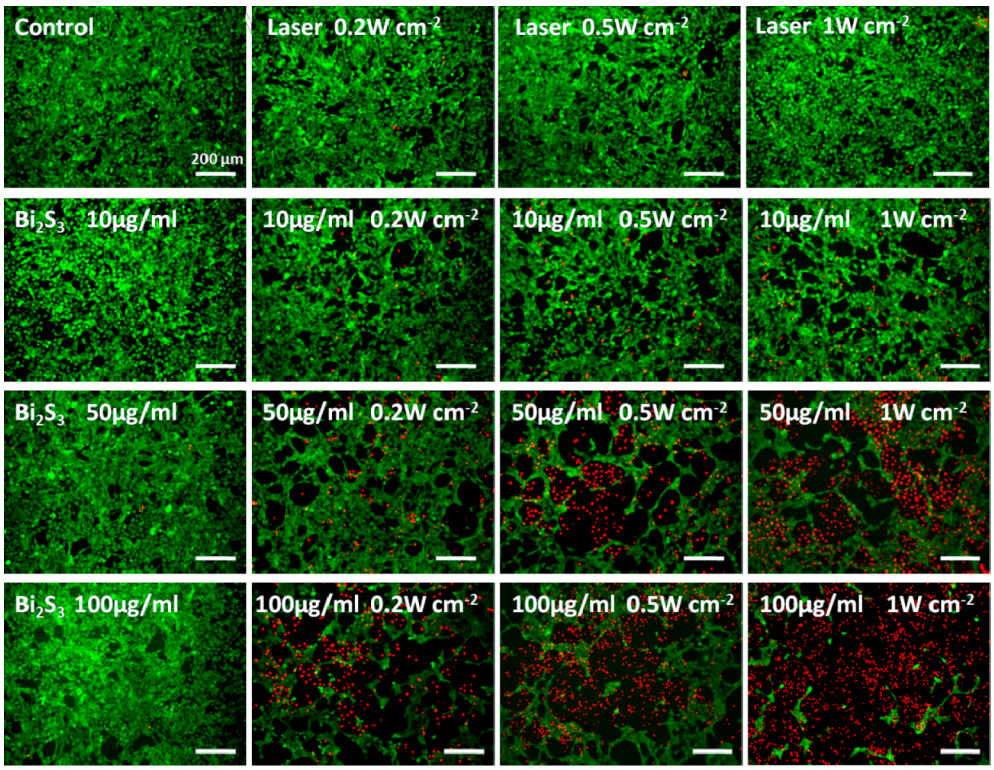

Figure 2. ***In vitro*** **photothermal effect. Live−dead staining of 4T1 cells. 4T1 cells were incubated with different concentrations of Bi_2S_3 NRs for 24 h and irradiated for 8 min using an 808 nm laser with three different power densities.**

increased (Figure 1g), which indicates the efficient uptake of Bi_2S_3 NRs by cells. Intracellular distribution was further visualized by dark-field imaging. The control cells without Bi_2S_3 NRs showed no obvious signals under dark-field scattering microscopy. However, after incubation with 50 and 100 μg mL^{-1} of the Bi_2S_3 NRs, respectively, the cells were saturated with the Bi_2S_3 NRs aggregations, which indicates efficient cellular internalization (Figure 1 h,i). These results also indicate that the Bi_2S_3 NRs can be used as a useful probe for dark-field optical imaging with the advantages of high spatial resolution, well photostability, and noneblink.[54−56] To evaluate the *in vitro* cytotoxicity of Bi_2S_3 NRs with or without NIR laser exposure, the standard methyl thiazolyl tetrazolium (MTT) assay and live/dead staining were conducted by using 4T1 cell lines. The cell viability was not influenced by the mere presence of the NRs for concentrations up to 300 μg mL^{-1}, which verified that the Bi_2S_3 NRs possess low cytotoxicity (Figure 1e). In contrast, upon the NIR laser exposure, cell viabilities decreased significantly as the concentration of Bi_2S_3 NRs or power density increased, and almost no cells remained alive at a concentration of 100 μg mL^{-1} (power density = 1 W cm^{-2}) (Figure 1f and Figure 2), which indicates their high photothermal killing ability of cancer cells upon NIR irradiation. To make clear the cell death mechanism after photothermal treatment, an Annexin-V-FITC/PI method was conducted by flow cytometry. Figure 3 shows the flow cytometry graphs of the cells treated by Bi_2S_3 NRs with and without laser irradiation. Annexin-V-FITC emission signal was plotted on the *x*-axis, while PI emission signal was plotted on the *y*-axis. The quantities of living cells, early apoptosis cells, and late apoptosis/necrosis cells were determined by the percentage of Annexin V$^-$/PI$^-$, Annexin V$^+$/PI$^-$, Annexin V$^-$/PI$^+$, and Annexin V$^+$/PI$^+$. Almost no apoptosis or necrosis cells were observed in the group of no NIR treatment with the concentration of up to 100 μg mL^{-1}. When the concentration is 50 μg mL^{-1}, after laser irradiation, the early apoptosis rate of cells reached 20.7%, the late apoptosis/necrosis rate was 40.1%. When the concentration is 100 μg mL^{-1}, after laser irradiation, the early apoptosis rate of cells was 1.8%; the late apoptosis/necrosis rate reached 93.7%. The flow cytometry data revealed that cells upon photothermal treatment by Bi_2S_3 NRs showed irreversible damage, and the cells could no longer function or recover from the damage. The results showed that PTT treatment under relatively high temperature (~50 °C) more significantly induced 4T1 cell late apoptosis/necrosis (93.7%) as compared with PTT under a mild temperature of about 45 °C (40.1%).

Precise spatial- and temporal-specific monitoring of PTT agents *in vivo* is particularly demanded as it potentially opens a novel avenue in guiding the therapeutic process, monitoring therapeutic response, and avoiding the destruction induced by external laser radiation to surrounding healthy tissue, which consequently would reduce the associated side effects.

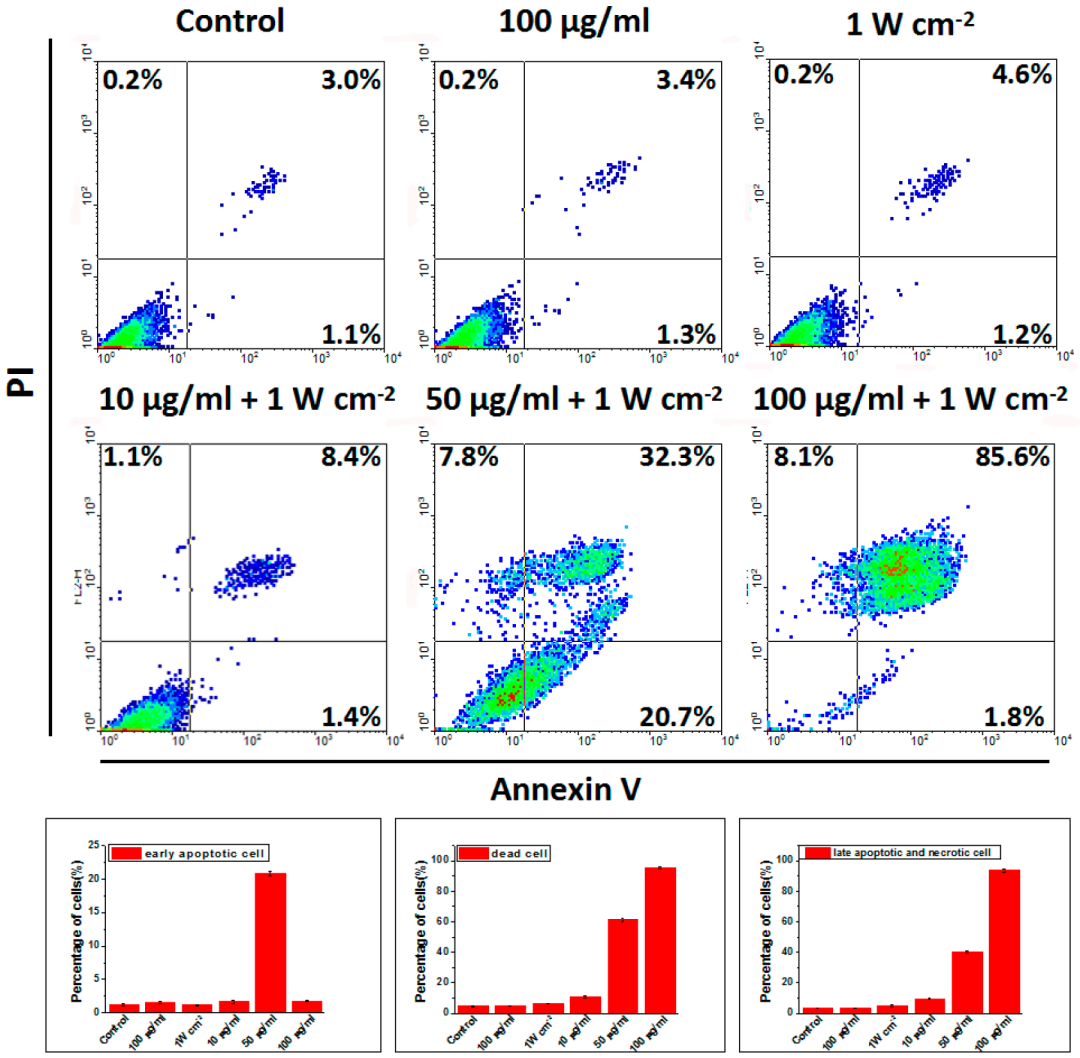

Figure 3. Flow cytometric profiles of 4T1 cells were examined to determine the percentages of apoptosis and late apoptosis/necrosis cells with different treatments. Statistical data of percentage of apoptosis, dead, and late apoptosis/necrosis cells under different treatments.

Therefore, we next employed the as-prepared Bi_2S_3 NRs as the efficient contrast agent for MSOT and CT imaging. MSOT is a new technology that largely overcomes the depth and resolution limits of optical imaging. MSOT is greatly welcomed to cross-sectional "listening" of entire tumors at depths not available to microscopy and sensitivity not available to CT imaging, arising from its high spatial resolution to soft tissues and real-time monitoring.[41,44] Herein, we first explored the Bi_2S_3 NRs as the MSOT contrast agent because of their high NIR absorption and efficient NIR photothermal conversion abilities. To examine MSOT imaging capability and monitor the trace of Bi_2S_3 NRs *in vivo*, tumor-bearing mice were intravenously (i.v.) injected with 200 μL of Bi_2S_3 NRs (2 mg mL^{-1}), and the cross-sectional photoacoustic (PA) signals of tumors were recorded at different time intervals. Before NRs injection, the MSOT image showed observable but weak PA signals (~1500 au) in the tumor region, which arise from the contrast of tumor blood. After NRs injection, the contrast in tumors remarkably enhanced, which indicates the gradual homing of NRs in tumors (Figure 4a–e). Quantifying PA signals showed a homing burst (3 h post injection, ~4270 au), and the signals lasted up to 24 h (Figure 4f). This result clearly shows that the Bi_2S_3 NRs have satisfactory residence time in tumor and are efficiently passively targeted to the tumor site. The surface coating and appropriate particles size favored efficient EPR effect may explain the significant passive targeting and long residence time in tumors. Besides the application for MSOT imaging, these Bi_2S_3 NRs could also be used as CT imaging contrast agents since they contain Bi atoms that have strong X-ray attenuation capability.[34,37] To assess the CT contrast performance of Bi_2S_3 NRs *in vitro*, Hounsfield units (HU) values were recorded with different NRs concentrations. The HU values increased linearly with the increase of concentrations of both Bi_2S_3 NRs and clinical iodine-based CT contrast agent (iopromide) (Figure S6). The slope of the HU value for Bi_2S_3 NRs

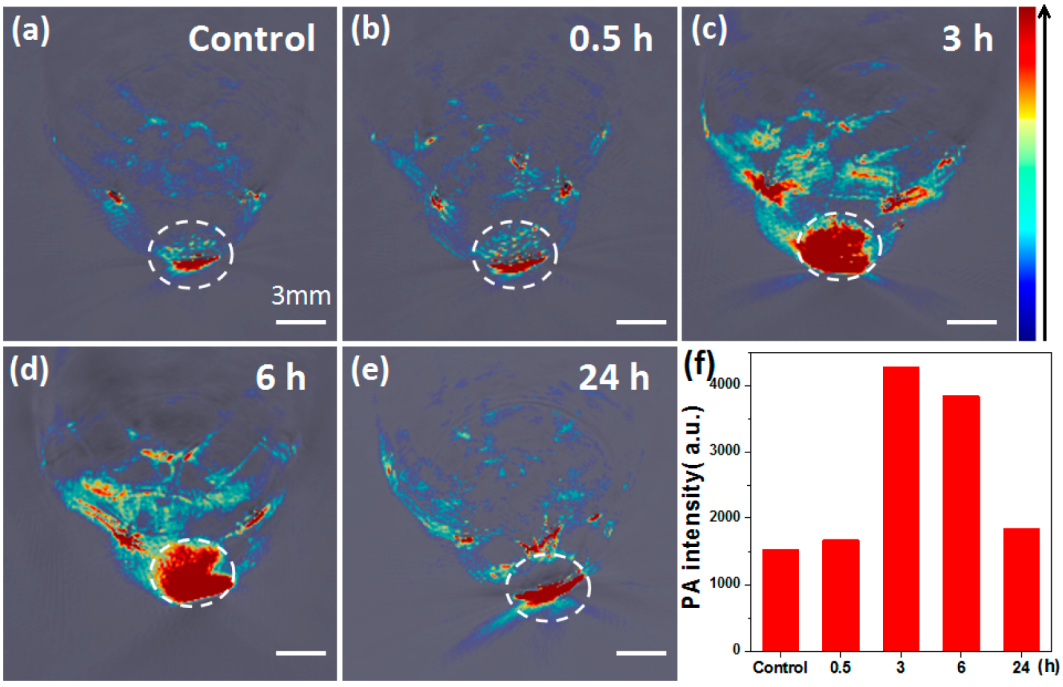

Figure 4. *In vivo* **MSOT imaging in 4T1 tumor-bearing mice. (a−e) MSOT images of tumor before and after i.v. injection with Bi_2S_3 NRs at different time points (0.5, 3, 6, and 24 h). (f) The intensity of photoacoustic signals in tumor at different time points.**

was about 39.36, and it is much higher than that of iopromide (16.38). This enhancement of the X-ray attenuation possibly results from the fact that Bi atoms have a higher X-ray absorption efficiency than that of iopromide (Bi, 5.74 cm^2/g; I, 1.94 cm^2/g at 100 keV, respectively).[57] To evaluate Bi_2S_3 NRs CT performance and visualize the NRs distribution in the whole body, we then conducted CT imaging in tumor-bearing mice at 5 min and 3 h post injection, respectively. Interestingly, the vasculature was hyperattenuating at an early stage after injection of Bi_2S_3 NRs and led to a clear angiography with contrast filling of the heart, vena cava, pulmonary vein plexus, vena epigastrica, tumor surface vascularity, and tumor microvessels (Figure 5b,d; Video S1 in the Supporting Information). The tumor vessels possessing irregular and surficial spatial distribution spring from the branch of abdominal veins. The rapid growth of tumor angiogenesis results in the tortuous, leaky, and irregular architecture of tumor blood vessels. This defective vasculature leads to the EPR effect that can be used for the NPs preferentially accumulating at the tumor site.[58−60] Thus, achieving such 3D imaging of tumor-associated vessels is the heavy focus in design of precision nanomedicine that can be taken advantage of for the guidance of tumor targeting and embolization. In addition, vascular pathema has become one of the serious diseases that threatens the health of the middle- and old-aged people. Therefore, Bi_2S_3 NRs could be a well favorable candidate for vascular disease diagnosis and effective cancer therapy. Accompanied with the extension of the NRs circulation time in blood, the NRs gradually accumulated in the tumor site. After 3 h post Bi_2S_3 NRs injection, Figure 5, panel c showed the remarkable CT contrast signals in tumors, which confirms the sufficient accumulation of Bi_2S_3 NRs in tumors, which guarantees the further application in PTT (Video S2 in the Supporting Information). The tumor-homing effect shown in CT was consistent with the MSOT results, which further confirms the efficient passive targeting ability of Bi_2S_3 NRs to tumors. In addition, we could observe clear contrast enhancement of liver and spleen, which suggests that NRs were accumulated *via* reticuloendothelial systems (RES) absorption and further metabolized in the liver and spleen.[61,62] Thus, Bi_2S_3 NRs have remarkable MSOT/CT imaging capabilities and obvious tumor-homing effects.

Having precisely monitored the trace and obvious tumor-homing effect of Bi_2S_3 NRs, we then investigated their PTT performance *in vivo*. When the tumor sizes reached approximately 100 mm^3, the male 4T1 tumor-bearing mice were divided into four groups: (a) PBS injection; (b) laser only; (c) Bi_2S_3 NRs i.v. injection; and (d) Bi_2S_3 NRs (i.v. injection) + laser. Male 4T1 tumor-bearing mice received an injection of Bi_2S_3 NRs (dose = 20 mg kg^{-1}) and then were exposed to 808 nm NIR laser (power density = 1 W cm^{-2}) for 15 min. The temperature of the tumor area was recorded by an IR thermal camera at specific time intervals (Figure 6a,b). Under NIR irradiation, the tumor surface temperature of the group (d) rapidly increased from ∼29 °C to ∼68 °C, which was capable of inducing hyperthermia to kill cancer cells. In contrast, the temperature of the tumor site of the control group and surrounding normal

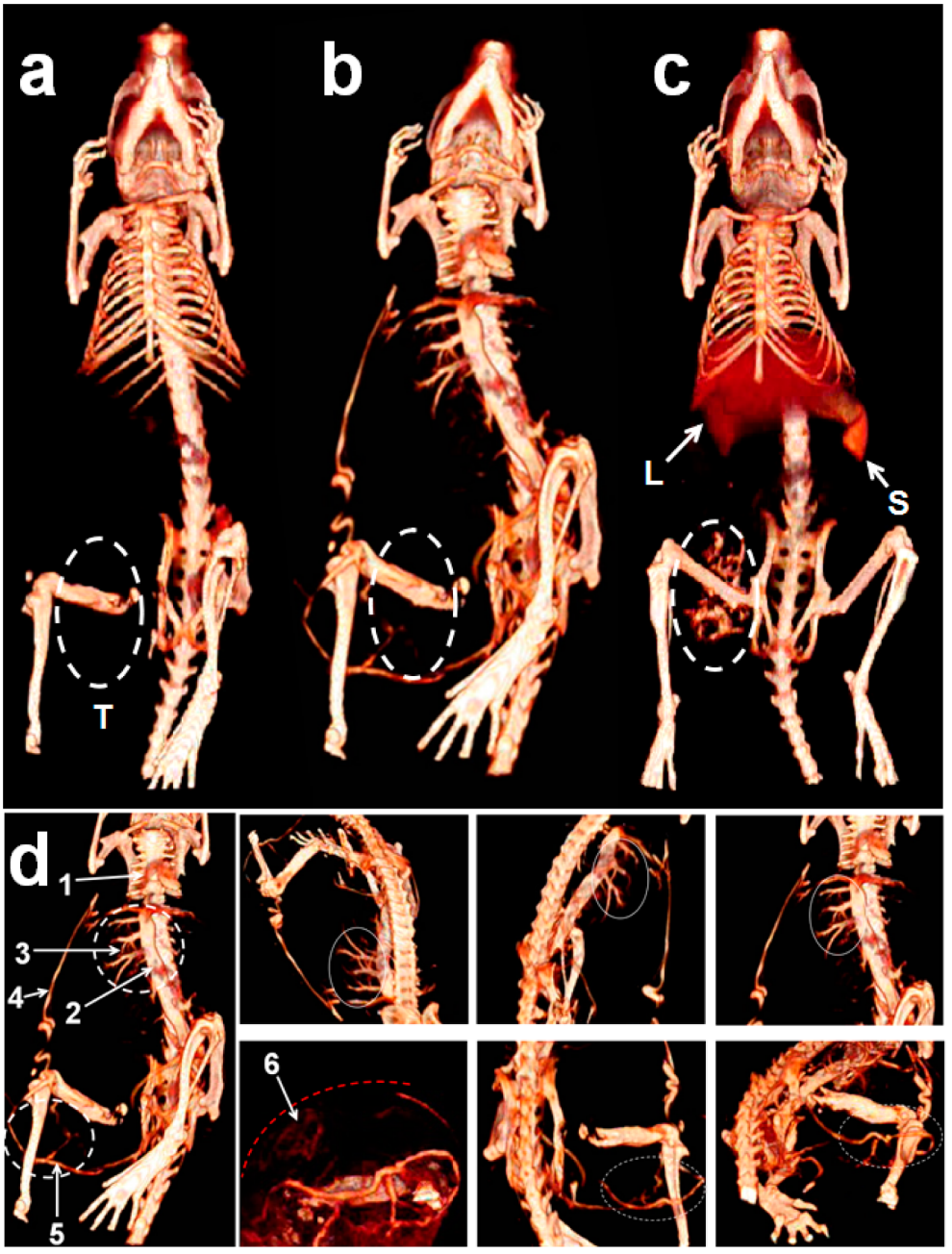

Figure 5. *In vivo* X-ray CT imaging in 4T1 tumor-bearing mice. (a) CT images of mice before injection. (b) CT images of mice 5 min post i.v. injection with Bi_2S_3 NRs. (c) CT images of mice 3 h post i.v. injection with Bi_2S_3 NRs: liver (L), spleen (S), and tumor (T). (d) Detailed CT images of the mice 5 min post i.v. injection to highlight the vascular structures: 1, heart; 2, vena cava; 3, pulmonary vein plexus; 4, vena epigastrica; 5, tumor surface vasculaity (from the abdominal venous branch); 6. tumor microvessel (TMV).

tissues in all experiment groups showed mild temperature change.

The tumor volumes of each group were measured and plotted as a function of time (Figure 6c). Tumors in the control groups grew rapidly. In contrast, the group (d) showed efficient tumor inhibition and complete eradication of tumors after 14 days PTT, leaving black scars at the initial tumor sites (Figure 6e). The tumor photograph and mean tumor weights in each group were shown in Figure 6, panels d and f. The mean tumor weight in group treated with Bi_2S_3 NRs (i.v. injection) + laser was the lightest among all the groups. These results reveal that PTT based on Bi_2S_3 NRs can realize completed tumor destruction and without regrowth in our observation period. Moreover, the efficient photothermal ablation of primary tumors can effectively preclude its metastasis. Presenting in the pathological examination by haematoxylin and eosin (HE) staining (Figure 6g) is no noticeable sign of pulmonary metastasis in photothermal treatment group (group d), while a large number of metastasis sites in the lungs of the other three control groups were

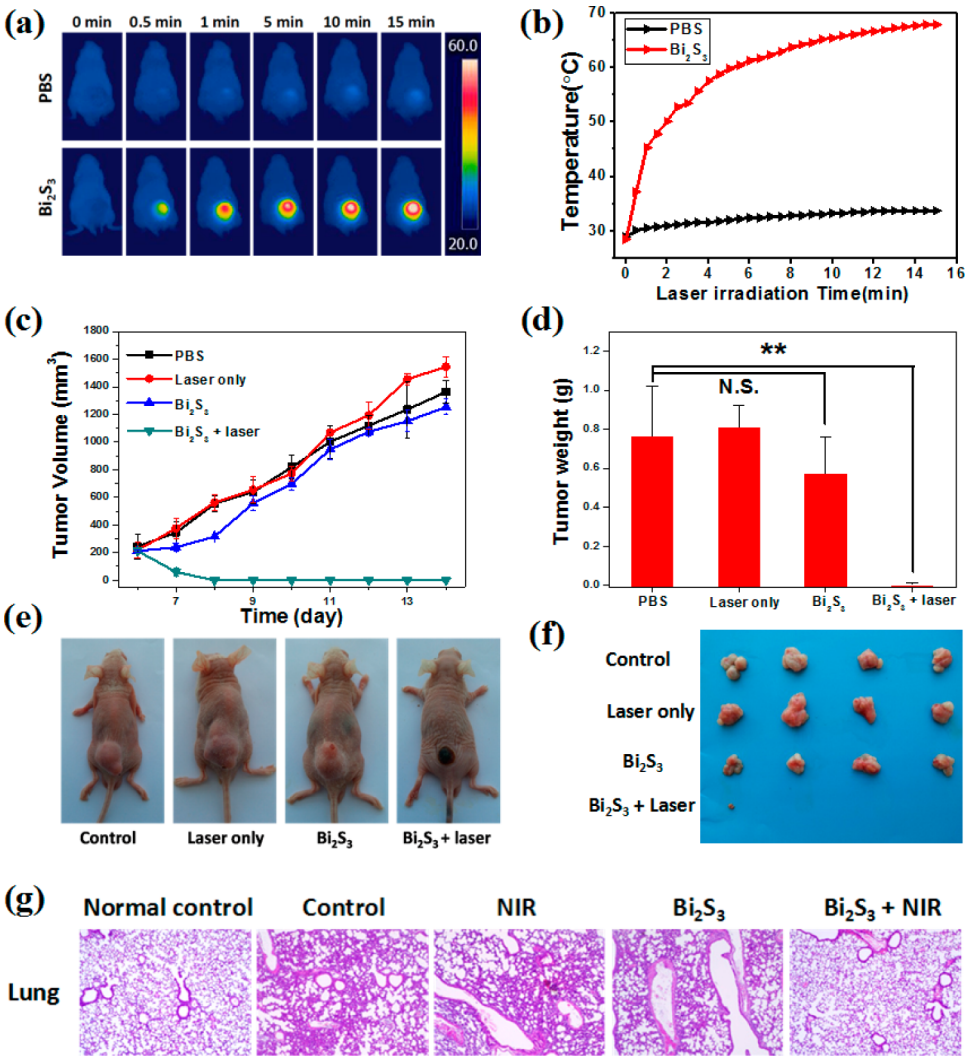

Figure 6. *In vivo* **photothermal therapy. (a, b) NIR photothermal images of 4T1 tumor-bearing mice with i.v. injection of PBS and Bi_2S_3 NRs (dose = 20 mg kg^{-1}) under the 808 nm laser irradiation taken at different time intervals. The laser power density was 1 W cm^{-2}. (c) Tumor volume growth curves of different groups of mice after various treatments (four mice for each group). Groups: (a) PBS injection; (b) laser only; (c) Bi_2S_3 NRs i.v. injection; and (d) Bi_2S_3 NRs (i.v. injection) + laser. (d) Average weights of tumors collected from the mice at the end of photothermal therapy. *P* values: ** $p < 0.01$, N.S. (no significant difference) $p > 0.05$, are calculated by *t* test. (e) Representative photos of mice after different treatments indicated taken 14 days after treatment. Error bars correspond to mean ± standard deviations. (f) Photos of tumors collected from different groups of mice at the end of treatment. (g) No obvious tumor metastases in the Bi_2S_3 NRs + laser group by HE staining.**

found. Nanomaterials-based photothermal treatment of cancer may be advantageous with respect to triggering the adaptive immunological responses against tumor cells in the body, thereafter contributing to tumor metastasis inhibition.[63−68] Our results provide a feasible vision to preclude that cancer metastasis by NPs induced efficient photoablation of the primary tumor upon NIR irradiation. Taken together, Bi_2S_3 NRs hold great potentials as an ideal agent for *in vivo* photothermal ablation of tumors and effective tumor metastasis inhibition.

Safety of the nanomedicine is an essential concern when it comes to the design of nanomaterials for biomedical applications.[69−71] Therefore, we then conducted a series of experiments *in vivo*, including the body weight, biodistribution, major organ weight, and blood biochemistry analysis, to ensure the safe application of Bi_2S_3 NRs. Our results indicate that no obvious signs of mouse abnormal behavior, weight loss, and weight of major organs and tissues were noticed (Figure S8). The hepatic function markers (ALT, AST) and renal function markers (CREA, UA, and BUN) were measured to be normal, which indicates no noticeable hepatic and renal dysfunction induced by Bi_2S_3 NRs treatment (Table S1). The MSOT/CT and biodistribution (Figure S9) results reported that the NRs presented appreciable localization in the liver. However, the *in vivo* toxicity assess profiles confirmed that the liver was unaffected by the accumulation of Bi_2S_3 NRs at least in short-term. These preliminary results proved that Bi_2S_3 NRs at the given dose hardly cause *in vivo* toxicity effects.

CONCLUSION

In summary, we have successfully presented a precision nanomedicine based on Bi_2S_3 NRs designed specifically for MSOT/CT spatial- and temporal-specifically guided PTT. The as-prepared Bi_2S_3 NRs possessing ideal photothermal effect and MSOT/CT imaging capability simultaneously act as "satellite" and "precision targeted weapon" triggered by NIR for the precise destruction of tumors, realizing complete primary tumor destruction, and metastasis inhibition. Toxicity screening confirmed that Bi_2S_3 NRs possess well biocompatibility. Overall, although more detailed investigations are still awaited to understand the pharmacokinetics, pharmacodynamics, and long-term toxicity, this simple but powerful theranostic nanomaterial shows a potential promise for precision nanomedicine paradigm and other disease precise manipulation.

EXPERIMENTAL SECTION

Materials. All chemicals, unless specified otherwise, were purchased from Sigma-Aldrich and used as received without further purification. Calcein-AM (CA), and propidium iodide (PI) were provided by Dojindo Laboratories in Japan. All the chemicals were used as received without further purification. DI water was obtained by an 18-MΩ (SHRO-plus DI) system.

Synthesis of OA-Coated Bi_2S_3 NRs. The OA-Bi_2S_3 NRs were prepared by a facile solvothermal method. In a typical synthesis route, 1.45 g of bismuth neodecanoate was added to a mixture of OA (20 mL) and ethanol (10 mL) under thorough stirring. Then, 4 mL of oleyl amine solution containing thioacetamide (0.15 g) was quickly added to the mixture. After vigorous stirring for 30 min, the colloidal solution was transferred into a 50 mL Teflon-lined autoclave, sealed, and heated at 150 °C for 10 h. The systems were then allowed to naturally cool to room temperature. The final products were collected by centrifugation and washed with ethanol several times to remove any possible remnants.

Preparation of Tween-Functionalized Bi_2S_3 NRs. To transfer Bi_2S_3 NRs from an organic phase to an aqueous phase, a biocompatible amphiphilic polymer Tween 20 was adopted to functionalize the as-prepared NRs.[72,73] In a typical procedure, 50 mg of OA-Bi_2S_3 NRs and 100 μL of Tween 20 were well dispersed in 20 mL of cyclohexane while being stirred at room temperature for 1 h. Then, the dispersion was added dropwise into 30 mL of DI water under stirring contained in a 100 mL flask placed in a 70 °C water bath and maintained for 3 h to evaporate the cyclohexane. The Tween 20-functionalized Bi_2S_3 NRs were obtained by centrifugation and washed with ethanol several times.

Characterization. The morphology and size of the as-synthesized NPs were characterized by the field emission scanning electron microscope (FE-SEM) and TEM (Tecnai G2 F20 U-TWIN operated at 200 kV). Powder XRD patterns of the dried products were measured using a Japan Rigaku D/max-2500 diffractometer with Cukα radiation (λ = 1.5418 Å). All photos of UCL were acquired by a Nikon D3100 digital camera. FTIR spectra were carried out by a Fourier transform Bruker EQUINOX55 spectrometer with the KBr pellet technique.

***In Vitro* Cytotoxicity Study.** Murine breast carcinoma cell line 4T1 was maintained in RPMI 1640 medium (WISENT Inc.) supplemented with 10% fetal bovine serum (WISENT Inc.) and 1% penicillin−streptomycin (WISENT Inc.) at 37 °C in a humidified atmosphere of 5% CO_2. Cell viability was determined by a MTT method. First, 3000 cells were plated in 96-well microplates (Costar, Corning, NY). After incubation for 24 h, cells were incubated with a series of concentrations of Bi_2S_3 NRs (0, 1, 5, 10, 20, 50, 100, 200, and 300 μg mL^{-1}) for 24 h, respectively. Meanwhile, the wells unexposed to any samples were regarded as control. The MTT test was performed immediately after treatment of the cells or after incubation.

Inductively Coupled Plasma Mass Spectrometry (ICP-MS) for Bi Element Quantification. To quantify the cellular uptake of Bi_2S_3 NRs, 4T1 cells were seeded into 6-well plates with complete 1640 medium at a density of 2×10^5 cells/mL for 24 h, then the medium was removed and replaced with the complete medium, respectively, containing 20 and 50 μg mL^{-1} Bi_2S_3 NRs. Meanwhile, the cells were incubated with different time slices, including 1, 3, 6, 12, 24, and 48 h, four wells at each time point. Cells were lightly washed three times with PBS, digested with 0.25% trypsin containing 0.02% EDTA, centrifuged for 15 min at 1500 rpm, collected, and counted. To study biodistribution of Bi_2S_3 NRs in BALB/c mice, 200 μL of Bi_2S_3 NRs (2 mg mL^{-1}) suspension was i.v. injected into the tail vein. At 24 h post administration, mice were sacrificed and organs dissected and weighed. Tissue samples from above were stored at −20 °C before analysis. For ICP-MS experiments, the above each sample was added 5 mL of HNO_3, transferred to flasks, and sealed for predigestion overnight. The next day, 3 mL of 30% H_2O_2 was added to each flask. The flasks were placed onto a hot plate and maintained at 150 °C for 3 h until digestion was complete and then cooled to room temperature. The solution in each flask was diluted to 3 g with 2% HNO_3. A series of Bi standard solutions (0, 0.5, 1, 5, 10, 50, and 100 ppb) was prepared with the above solution. Both standard and test solutions were measured by ICP-MS (Thermal Elemental X7, Thermal Fisher Scientific Inc., USA). The amount of Bi_2S_3 NRs was finally normalized to the cell number or tissue weight per gram.

Dark-Field Imaging for Cellular Uptake Quantitation. The 4T1 cells were seeded on glass-bottom dishes for 24 h to allow the cells to attach. Final concentrations of 50 and 100 μg mL^{-1} Bi_2S_3 NRs were added to the cells and coincubated for 24 h. Next, cells were washed gently with PBS three times and fixed with formalin for 15 min. The light scattering images were recorded using an inverted fluorescence microscope (Nikon Eclipse Ti−S, Nikon Instruments Inc., USA) observed with a highly numerical dark-field condenser.

***In Vitro* Photothermal Therapy.** To study the photothermal therapy effect of Bi_2S_3 NRs, 4T1 cells were seeded in 6-well plates with a density of 5×10^4 for 12 h and set four groups (control, laser only, Bi_2S_3 NRs, Bi_2S_3 NRs + laser). When cells had grown to 80% in plates, the first group had no treatment, the second one was just irradiated with different power density (0.2, 0.5, 1 W cm^{-2}) for 8 min, the third one was incubated with different concentrations of Bi_2S_3 NRs (10, 50, and 100 μg mL^{-1}) for 24 h, at the same time, irradiated with different power densities (0.2, 0.5, 1 W cm^{-2}) for 8 min, respectively. All cells were stained by LIVE−DEAD kits after the treatment and observed using fluorescence microscope (10 X), and live cells showed green color and dead ones exhibited red color. Furthermore, cells treated by different concentrations of Bi_2S_3 NRs (10, 50, and 100 μg mL^{-1}) for 24 h with NIR (1 W cm^{-2}) for 8 min were collected, washed three times with PBS, dyed with Annexin V-FITC/PI kit, and then detected by flow cytometry to make clear the cell death mode.

Animals. Male BALB/c nude mice were obtained from Beijing Vitalriver Experimental Animal Technology Co. Ltd. with body weights of 19−21 g and housed in stainless steel cages under the standard conditions (20 ± 2 °C room temperature, 60 ± 10% relative humidity) with a 12 h light/dark cycle. Distilled water and sterilized food for mice were available *ad libitum*. Animals were acclimated to this environment for 5 days prior to treatment. All procedures used in this experiment were compliant with the local animal ethics committee.

***In Vivo* MSOT Imaging.** A 200 μL sample of Bi_2S_3 NRs (2 mg mL^{-1}) suspension was i.v. injected into the tail vein of tumor-bearing BALB/c nude mice. After this injection, mice were scanned at different time intervals postinjection, that is, 0.5, 3, 6, and 24 h with the MSOT (MSOT inVision 128, iThera medical, Germany) to collect signals. Photoacoustic signals

were recorded with different wavelength (680−900 nm) excitation light. The main experimental parameters were ten wavelengths for each slice from 680−900 nm, and the region of interest (ROI) is 20 mm. We got the MSOT signals before injection as control.

***In Vivo* CT Imaging.** *In vivo* CT imaging was performed on small mice X-ray CT (Gamma Medica-Ideas). Imaging parameters were as follows: field of view (78.92 mm × 78.92 mm), slice thickness 154 μm, effective pixel size 50 μm, tube voltage 80 kV, tube current 270 μA. The reconstruction was done by using the filtered back projection (FBP) method. The reconstruction kernel used a Feldkamp cone beam correction and SheppLogan filter. The CT images were analyzed using amira 4.1.2. In detail, tumor-bearing BALB/c nude mice were i.v. injected with 200 μL of Bi_2S_3 NRs (10 mg mL^{-1}) prior to imaging. After 5 and 180 min, tumor-bearing mice were imaged by a small animal X-ray CT. The mice whole body 360° scan lasted about 20 min.

Therapeutic Evaluation of Bi_2S_3 NRs in Tumor-Bearing Mice. Tumor-bearing mice were prepared by inoculating 1 × 10^6 4T1 cells at backside in male BALB/c nude mice. When the tumor sizes reached approximately 100 mm^3, the mice were divided into four groups: (a) PBS injection; (b) laser only; (c) Bi_2S_3 NRs i.v. injection; and (d) Bi_2S_3 NRs (i.v. injection) + laser. The 4T1 tumor-bearing mice were i.v. injected with Bi_2S_3 NRs (dose = 20 mg kg^{-1}) and exposed to an 808 nm laser (power density: 1 W cm^{-2}, 15 min) when the NRs reached the peak level in tumors (3 h post injection). Temperature change under laser irradiation in the tumor region was recorded by a NIR camera for different groups. Pictures were recorded at 0, 0.5, 1, 5, 10, and 15 min. Tumor growth and mouse weight were measured in the following days. The tumor sizes were measured by a caliper and calculated as follows:

$$V = ab^2/2$$

where V (mm^3) is the volume of the tumor, and a (mm) and b (mm) are the tumor length and tumor width, respectively. When the experiments were finished, the mice were sacrificed, and the tumors and major tissues were dissected and weighed to evaluate the therapeutic efficacy of different groups.

Blood Biochemistry and Pathology. The analysis of blood biochemical examination was carried out using blood collection by removal of the eyeball in the different treated mice above, and major organs from those mice were harvested, fixed in 10% neutral buffered formalin, processed routinely into paraffin, stained with HE, and pathology was examined by a microscope. For blood analysis, 1 mL of blood was collected from mice after 3 h standing in room temperature, which was separated by centrifugation into cellular and plasma fractions.

Conflict of Interest: The authors declare no competing financial interest.

Acknowledgment. This work was supported by the National Basic Research Programs of China (973 programs, Nos. 2012CB932504, 2012CB934003, and 2015CB932104), International Science and Technology Cooperation Program of China, Ministry of Science Technology of China (2013DFG32340), NSFC (Nos. 21001108, 11205166, and 21320102003), and the National Science Fund for Distinguished Young Scholars (No. 11425520).

Supporting Information Available: Additional figures and movies as described in the text. This material is available free of charge via the Internet at http://pubs.acs.org.

REFERENCES AND NOTES

1. Peer, D.; Karp, J. M.; Hong, S.; Farokhzad, O. C.; Margalit, R.; Langer, R. Nanocarriers as an Emerging Platform for Cancer Therapy. *Nat. Nanotechnol.* **2007**, *2*, 751–760.
2. Barreto, J. A.; O'Malley, W.; Kubeil, M.; Graham, B.; Stephan, H.; Spiccia, L. Nanomaterials: Applications in Cancer Imaging and Therapy. *Adv. Mater.* **2011**, *23*, 18–40.
3. Kievit, F. M.; Zhang, M. Cancer Nanotheranostics: Improving Imaging and Therapy by Targeted Delivery Across Biological Barriers. *Adv. Mater.* **2011**, *23*, 217–247.
4. Ma, X.; Zhao, Y.; Liang, X.-J. Theranostic Nanoparticles Engineered for Clinic and Pharmaceutics. *Acc. Chem. Res.* **2011**, *44*, 1114–1122.
5. Goldsmith, M.; Abramovitz, L.; Peer, D. Precision Nanomedicine in Neurodegenerative Diseases. *ACS Nano* **2014**, *8*, 1958–1965.
6. Alivisatos, A. P.; Andrews, A. M.; Boyden, E. S.; Chun, M.; Church, G. M.; Deisseroth, K.; Donoghue, J. P.; Fraser, S. E.; Lippincott-Schwartz, J.; Looger, L. L.; et al. Nanotools for Neuroscience and Brain Activity Mapping. *ACS Nano* **2013**, *7*, 1850–1866.
7. Sun, Y.; Zhu, X.; Peng, J.; Li, F. Core−Shell Lanthanide Upconversion Nanophosphors as Four-Modal Probes for Tumor Angiogenesis Imaging. *ACS Nano* **2013**, *7*, 11290–11300.
8. Jing, L.; Liang, X.; Deng, Z.; Feng, S.; Li, X.; Huang, M.; Li, C.; Dai, Z. Prussian Blue Coated Gold Nanoparticles for Simultaneous Photoacoustic/CT Bimodal Imaging and Photothermal Ablation of Cancer. *Biomaterials* **2014**, *35*, 5814–5821.
9. Dong, K.; Liu, Z.; Li, Z.; Ren, J.; Qu, X. Hydrophobic Anticancer Drug Delivery by a 980 nm Laser-Driven Photothermal Vehicle for Efficient Synergistic Therapy of Cancer Cells *in Vivo*. *Adv. Mater.* **2013**, *25*, 4452–4458.
10. Huang, P.; Lin, J.; Li, W.; Rong, P.; Wang, Z.; Wang, S.; Wang, X.; Sun, X.; Aronova, M.; Niu, G.; Leapman, R. D.; Nie, Z.; Chen, X. Biodegradable Gold Nanovesicles with an Ultrastrong Plasmonic Coupling Effect for Photoacoustic Imaging and Photothermal Therapy. *Angew. Chem., Int. Ed.* **2013**, *52*, 13958–13964.
11. Huang, X.; El-Sayed, I. H.; Qian, W.; El-Sayed, M. A. Cancer Cell Imaging and Photothermal Therapy in the Near-Infrared Region by Using Gold Nanorods. *J. Am. Chem. Soc.* **2006**, *128*, 2115–2120.
12. El-Sayed, I. H.; Huang, X.; El-Sayed, M. A. Selective Laser Photothermal Therapy of Epithelial Carcinoma Using Anti-EGFR Antibody Conjugated Gold Nanoparticles. *Cancer Lett.* **2006**, *239*, 129–135.
13. Tian, G.; Zhang, X.; Zheng, X.; Yin, W.; Ruan, L.; Liu, X.; Zhou, L.; Yan, L.; Li, S.; Gu, Z.; et al. Multifunctional Rb_xWO_3 Nanorods for Simultaneous Combined Chemophotothermal Therapy and Photoacoustic/CT Imaging. *Small* **2014**, *10*, 4160–4170.
14. Zhang, Z.; Wang, L.; Wang, J.; Jiang, X.; Li, X.; Hu, Z.; Ji, Y.; Wu, X.; Chen, C. Mesoporous Silica-Coated Gold Nanorods as a Light-Mediated Multifunctional Theranostic Platform for Cancer Treatment. *Adv. Mater.* **2012**, *24*, 1418–1423.
15. Yin, W.; Yan, L.; Yu, J.; Tian, G.; Zhou, L.; Zheng, X.; Zhang, X.; Yong, Y.; Li, J.; Gu, Z.; et al. High-Throughput Synthesis of Single-Layer MoS_2 Nanosheets as a Near-Infrared Photothermal-Triggered Drug Delivery for Effective Cancer Therapy. *ACS Nano* **2014**, *8*, 6922–6933.
16. Zhang, Z.; Wang, J.; Nie, X.; Wen, T.; Ji, Y.; Wu, X.; Zhao, Y.; Chen, C. Near-Infrared Laser-Induced Targeted Cancer Therapy Using Thermoresponsive Polymer Encapsulated Gold Nanorods. *J. Am. Chem. Soc.* **2014**, *136*, 7317–7326.
17. Zha, Z.; Wang, J.; Qu, E.; Zhang, S.; Jin, Y.; Wang, S.; Dai, Z. Polypyrrole Hollow Microspheres as Echogenic Photothermal Agent for Ultrasound Imaging Guided Tumor Ablation. *Sci. Rep.* **2013**, *3*, 2360.
18. Liu, T.; Wang, C.; Gu, X.; Gong, H.; Cheng, L.; Shi, X.; Feng, L.; Sun, B.; Liu, Z. Drug Delivery with PEGylated MoS_2 Nanosheets for Combined Photothermal and Chemotherapy of Cancer. *Adv. Mater.* **2014**, *26*, 3433–3440.
19. Jin, Y.; Li, Y.; Ma, X.; Zha, Z.; Shi, L.; Tian, J.; Dai, Z. Encapsulating Tantalum Oxide into Polypyrrole Nanoparticles for X-ray CT/Photoacoustic Bimodal Imaging-Guided Photothermal Ablation of Cancer. *Biomaterials* **2014**, *35*, 5795–5804.
20. Dong, K.; Liu, Z.; Li, Z. H.; Ren, J. S.; Qu, X. G. Hydrophobic Anticancer Drug Delivery by a 980 nm Laser-Driven Photothermal Vehicle for Efficient Synergistic Therapy of Cancer Cells *in Vivo*. *Adv. Mater.* **2013**, *25*, 4452–4458.
21. Lovell, J. F.; Jin, C. S.; Huynh, E.; Jin, H.; Kim, C.; Rubinstein, J. L.; Chan, W. C. W.; Cao, W.; Wang, L. V.; Zheng, G.

Porphysome Nanovesicles Generated by Porphyrin Bilayers for Use as Multimodal Biophotonic Contrast Agents. *Nat. Mater.* **2011**, *10*, 324–332.
22. Cheng, L.; Liu, J.; Gu, X.; Gong, H.; Shi, X.; Liu, T.; Wang, C.; Wang, X.; Liu, G.; Xing, H.; et al. PEGylated WS_2 Nanosheets as a Multifunctional Theranostic Agent for *in Vivo* Dual-Modal CT/Photoacoustic Imaging Guided Photothermal Therapy. *Adv. Mater.* **2014**, *26*, 1886–1893.
23. Nie, L.; Wang, S.; Wang, X.; Rong, P.; Ma, Y.; Liu, G.; Huang, P.; Lu, G.; Chen, X. *In Vivo* Volumetric Photoacoustic Molecular Angiography and Therapeutic Monitoring with Targeted Plasmonic Nanostars. *Small* **2014**, *10*, 1585–1593.
24. Gu, Z.; Yan, L.; Tian, G.; Li, S.; Chai, Z.; Zhao, Y. Recent Advances in Design and Fabrication of Upconversion Nanoparticles and Their Safe Theranostic Applications. *Adv. Mater.* **2013**, *25*, 3758–3779.
25. Tian, Q.; Hu, J.; Zhu, Y.; Zou, R.; Chen, Z.; Yang, S.; Li, R.; Su, Q.; Han, Y.; Liu, X. Sub-10 nm Fe_3O_4@$Cu_{2-x}S$ Core–Shell Nanoparticles for Dual-Modal Imaging and Photothermal Therapy. *J. Am. Chem. Soc.* **2013**, *135*, 8571–8577.
26. Jin, C. S.; Lovell, J. F.; Chen, J.; Zheng, G. Ablation of Hypoxic Tumors with Dose-Equivalent Photothermal, but Not Photodynamic, Therapy Using a Nanostructured Porphyrin Assembly. *ACS Nano* **2013**, *7*, 2541–2550.
27. Tian, Q.; Jiang, F.; Zou, R.; Liu, Q.; Chen, Z.; Zhu, M.; Yang, S.; Wang, J.; Wang, J.; Hu, J. Hydrophilic Cu_9S_5 Nanocrystals: A Photothermal Agent with a 25.7% Heat Conversion Efficiency for Photothermal Ablation of Cancer Cells *in Vivo*. *ACS Nano* **2011**, *5*, 9761–9771.
28. Moon, H. K.; Lee, S. H.; Choi, H. C. *In Vivo* Near-Infrared Mediated Tumor Destruction by Photothermal Effect of Carbon Nanotubes. *ACS Nano* **2009**, *3*, 3707–3713.
29. Ayala-Orozco, C.; Urban, C.; Knight, M. W.; Urban, A. S.; Neumann, O.; Bishnoi, S. W.; Mukherjee, S.; Goodman, A. M.; Charron, H.; Mitchell, T.; et al. Au Nanomatryoshkas as Efficient Near-Infrared Photothermal Transducers for Cancer Treatment: Benchmarking against Nanoshells. *ACS Nano* **2014**, *8*, 6372–6381.
30. Jung, H. S.; Kong, W. H.; Sung, D. K.; Lee, M.-Y.; Beack, S. E.; Keum, D. H.; Kim, K. S.; Yun, S. H.; Hahn, S. K. Nanographene Oxide-Hyaluronic Acid Conjugate for Photothermal Ablation Therapy of Skin Cancer. *ACS Nano* **2014**, *8*, 260–268.
31. Sotiriou, G. A.; Starsich, F.; Dasargyri, A.; Wurnig, M. C.; Krumeich, F.; Boss, A.; Leroux, J.-C.; Pratsinis, S. E. Photothermal Killing of Cancer Cells by the Controlled Plasmonic Coupling of Silica-Coated Au/Fe_2O_3 Nanoaggregates. *Adv. Funct. Mater.* **2014**, *24*, 2818–2827.
32. Yu, J.; Yang, C.; Li, J.; Ding, Y.; Zhang, L.; Yousaf, M. Z.; Lin, J.; Pang, R.; Wei, L.; Xu, L.; et al. Multifunctional Fe_5C_2 Nanoparticles: A Targeted Theranostic Platform for Magnetic Resonance Imaging and Photoacoustic Tomography-Guided Photothermal Therapy. *Adv. Mater.* **2014**, *26*, 4114–4120.
33. Lusic, H.; Grinstaff, M. W. X-ray-Computed Tomography Contrast Agents. *Chem. Rev.* **2012**, *113*, 1641–1666.
34. Liu, Y.; Ai, K.; Lu, L. Nanoparticulate X-ray Computed Tomography Contrast Agents: From Design Validation to *in Vivo* Applications. *Acc. Chem. Res.* **2012**, *45*, 1817–1827.
35. Oh, M. H.; Lee, N.; Kim, H.; Park, S. P.; Piao, Y.; Lee, J.; Jun, S. W.; Moon, W. K.; Choi, S. H.; Hyeon, T. Large-Scale Synthesis of Bioinert Tantalum Oxide Nanoparticles for X-ray Computed Tomography Imaging and Bimodal Image-Guided Sentinel Lymph Node Mapping. *J. Am. Chem. Soc.* **2011**, *133*, 5508–5515.
36. Rabin, O.; Manuel Perez, J.; Grimm, J.; Wojtkiewicz, G.; Weissleder, R. An X-ray Computed Tomography Imaging Agent Based on Long-Circulating Bismuth Sulphide Nanoparticles. *Nat. Mater.* **2006**, *5*, 118–122.
37. Ai, K.; Liu, Y.; Liu, J.; Yuan, Q.; He, Y.; Lu, L. Large-Scale Synthesis of Bi_2S_3 Nanodots as a Contrast Agent for *in Vivo* X-ray Computed Tomography Imaging. *Adv. Mater.* **2011**, *23*, 4886–4891.
38. Ke, H.; Yue, X.; Wang, J.; Xing, S.; Zhang, Q.; Dai, Z.; Tian, J.; Wang, S.; Jin, Y. Gold Nanoshelled Liquid Perfluorocarbon Nanocapsules for Combined Dual-Modal Ultrasound/CT Imaging and Photothermal Therapy of Cancer. *Small* **2014**, *10*, 1220–1227.
39. Dong, W.; Li, Y.; Niu, D.; Ma, Z.; Liu, X.; Gu, J.; Zhao, W.; Zheng, Y.; Shi, J. A Simple Route To Prepare Monodisperse Au NP-Decorated, Dye-doped, Superparamagnetic Nanocomposites for Optical, MR, and CT Trimodal Imaging. *Small* **2013**, *9*, 2500–2508.
40. Fan, Q.; Cheng, K.; Hu, X.; Ma, X.; Zhang, R.; Yang, M.; Lu, X.; Xing, L.; Huang, W.; Gambhir, S. S. Transferring Biomarker into Molecular Probe: Melanin Nanoparticle as a Naturally Active Platform for Multimodality Imaging. *J. Am. Chem. Soc.* **2014**, *136* (43), 15185–15194.
41. Wang, L. V.; Hu, S. Photoacoustic Tomography: *In Vivo* Imaging from Organelles to Organs. *Science* **2012**, *335*, 1458–1462.
42. Razansky, D.; Distel, M.; Vinegoni, C.; Ma, R.; Perrimon, N.; Koster, R. W.; Ntziachristos, V. Multispectral Optoacoustic Tomography of Deep-Seated Fluorescent Proteins *in Vivo*. *Nat. Photonics* **2009**, *3*, 412–417.
43. Rosenthal, A.; Jaffer, F. A.; Ntziachristos, V. Intravascular Multispectral Optoacoustic Tomography of Atherosclerosis: Prospects and Challenges. *Imaging Med.* **2012**, *4*, 299–310.
44. Ntziachristos, V.; Razansky, D. Molecular Imaging by Means of Multispectral Optoacoustic Tomography (MSOT). *Chem. Rev.* **2010**, *110*, 2783–2794.
45. Kircher, M. F.; de la Zerda, A.; Jokerst, J. V.; Zavaleta, C. L.; Kempen, P. J.; Mittra, E.; Pitter, K.; Huang, R.; Campos, C.; Habte, F.; et al. A Brain Tumor Molecular Imaging Strategy Using a New Triple-Modality MRI-Photoacoustic-Raman nanoparticle. *Nat. Med.* **2012**, *18*, 829–834.
46. Kinsella, J. M.; Jimenez, R. E.; Karmali, P. P.; Rush, A. M.; Kotamraju, V. R.; Gianneschi, N. C.; Ruoslahti, E.; Stupack, D.; Sailor, M. J. X-Ray Computed Tomography Imaging of Breast Cancer by Using Targeted Peptide-Labeled Bismuth Sulfide Nanoparticles. *Angew. Chem., Int. Ed.* **2011**, *50*, 12308–12311.
47. Zhang, X.-D.; Chen, J.; Min, Y.; Park, G. B.; Shen, X.; Song, S.-S.; Sun, Y.-M.; Wang, H.; Long, W.; Xie, J.; et al. Metabolizable Bi_2Se_3 Nanoplates: Biodistribution, Toxicity, and Uses for Cancer Radiation Therapy and Imaging. *Adv. Funct. Mater.* **2014**, *24*, 1718–1729.
48. Li, J.; Jiang, F.; Yang, B.; Song, X.-R.; Liu, Y.; Yang, H.-H.; Cao, D.-R.; Shi, W.-R.; Chen, G.-N. Topological Insulator Bismuth Selenide as a Theranostic Platform for Simultaneous Cancer Imaging and Therapy. *Sci. Rep.* **2013**, *3*, 1998.
49. Thomson, J. W.; Lawson, G.; O'Brien, P.; Klenkler, R.; Helander, M. G.; Petrov, S.; Lu, Z.-H.; Kherani, N. P.; Adronov, A.; Ozin, G. Flash Nanowelding: Investigation and Control of the Photothermal Response of Ultrathin Bismuth Sulfide Nanowire Films. *Adv. Mater.* **2010**, *22*, 4395–4400.
50. Martinez, L.; Bernechea, M.; de Arquer, F. P. G.; Konstantatos, G. Near IR-Sensitive, Non-Toxic, Polymer/Nanocrystal Solar Cells Employing Bi_2S_3 as the Electron Acceptor. *Adv. Energy Mater.* **2011**, *1*, 1029–1035.
51. Malakooti, R.; Cademartiri, L.; Akçakir, Y.; Petrov, S.; Migliori, A.; Ozin, G. A. Shape-Controlled Bi_2S_3 Nanocrystals and Their Plasma Polymerization into Flexible Films. *Adv. Mater.* **2006**, *18*, 2189–2194.
52. Sigman, M. B.; Korgel, B. A. Solventless Synthesis of Bi_2S_3 (Bismuthinite) Nanorods, Nanowires, and Nanofabric. *Chem. Mater.* **2005**, *17*, 1655–1660.
53. Ayala-Orozco, C.; Urban, C.; Knight, M. W.; Urban, A. S.; Neumann, O.; Bishnoi, S. W.; Mukherjee, S.; Goodman, A. M.; Charron, H.; Mitchell, T.; Shea, M.; et al. Au Nanomatryoshkas as Efficient Near-Infrared Photothermal Transducers for Cancer Treatment: Benchmarking against Nanoshells. *ACS Nano* **2014**, *8*, 6372–6381.
54. Raschke, G.; Kowarik, S.; Franzl, T.; Sonnichsen, C.; Klar, T. A.; Feldmann, J.; Nichtl, A.; Kurzinger, K. Biomolecular Recognition Based on Single Gold Nanoparticle Light Scattering. *Nano Lett.* **2003**, *3*, 935–938.
55. Xu, X.-H. N.; Brownlow, W. J.; Kyriacou, S. V.; Wan, Q.; Viola, J. J. Real-Time Probing of Membrane Transport in Living Microbial Cells Using Single Nanoparticle Optics and Live Cell Imaging. *Biochemistry* **2004**, *43*, 10400–10413.

56. Hill, D. J.; Pinion, C. W.; Christesen, J. D.; Cahoon, J. F. Waveguide Scattering Microscopy for Dark-Field Imaging and Spectroscopy of Photonic Nanostructures. *ACS Photonics* **2014**, *1*, 725–731.
57. Lee, N.; Choi, S. H.; Hyeon, T. Nano-Sized CT Contrast Agents. *Adv. Mater.* **2013**, *25*, 2641–2660.
58. Folkman, J. Tumor Angiogenesis: Therapeutic Implications. *N. Engl. J. Med.* **1971**, *285*, 1182–1186.
59. Plank, M. J.; Sleeman, B. D. Tumour-Induced Angiogenesis: A Review. *J. Theor. Med.* **2003**, *5*, 137–153.
60. Matsumura, Y.; Maeda, H. A New Concept for Macromolecular Therapeutics in Cancer Chemotherapy: Mechanism of Tumoritropic Accumulation of Proteins and the Antitumor Agent Smancs. *Cancer Res.* **1986**, *46*, 6387–6392.
61. Wang, B.; He, X.; Zhang, Z.; Zhao, Y.; Feng, W. Metabolism of Nanomaterials *in Vivo*: Blood Circulation and Organ Clearance. *Acc. Chem. Res.* **2012**, *46*, 761–769.
62. Attia, M. F.; Anton, N.; Chiper, M.; Akasov, R.; Anton, H.; Messaddeq, N.; Fournel, S.; Klymchenko, A. S.; Mély, Y.; Vandamme, T. F. Biodistribution of X-Ray Iodinated Contrast Agent in Nanoemulsions Is Controlled by the Chemical Nature of the Oily Core. *ACS Nano* **2014**, *8* (10), 10537–10550.
63. Carmeliet, P.; Jain, R. K. Principles and Mechanisms of Vessel Normalization for Cancer and Other Angiogenic Diseases. *Nat. Rev. Drug Discovery* **2011**, *10*, 417–427.
64. Schroeder, A.; Heller, D. A.; Winslow, M. M.; Dahlman, J. E.; Pratt, G. W.; Langer, R.; Jacks, T.; Anderson, D. G. Treating Metastatic Cancer with Nanotechnology. *Nat. Rev. Cancer* **2012**, *12*, 39–50.
65. Liang, C.; Diao, S.; Wang, C.; Gong, H.; Liu, T.; Hong, G.; Shi, X.; Dai, H.; Liu, Z. Tumor Metastasis Inhibition by Imaging-Guided Photothermal Therapy with Single-Walled Carbon Nanotubes. *Adv. Mater.* **2014**, *26*, 5646–5652.
66. Wang, C.; Xu, L.; Liang, C.; Xiang, J.; Peng, R.; Liu, Z. Immunological Responses Triggered by Photothermal Therapy with Carbon Nanotubes in Combination with Anti-CTLA-4 Therapy To Inhibit Cancer Metastasis. *Adv. Mater.* **2014**, *26* (48), 8154–8162.
67. Kang, S.-G.; Zhou, G.; Yang, P.; Liu, Y.; Sun, B.; Huynh, T.; Meng, H.; Zhao, L.; Xing, G.; Chen, C.; et al. Molecular Mechanism of Pancreatic Tumor Metastasis Inhibition by $Gd@C_{82}(OH)_{22}$ and Its Implication for *de Novo* Design of Nanomedicine. *Proc. Natl. Acad. Sci. U.S.A.* **2012**, *109*, 15431–15436.
68. Guo, L.; Yan, D. D.; Yang, D.; Li, Y.; Wang, X.; Zalewski, O.; Yan, B.; Lu, W. Combinatorial Photothermal and Immuno Cancer Therapy Using Chitosan-Coated Hollow Copper Sulfide Nanoparticles. *ACS Nano* **2014**, *8*, 5670–5681.
69. Rivera-Gil, P.; Jimenez De Aberasturi, D.; Wulf, V.; Pelaz, B.; Del Pino, P.; Zhao, Y.; De La Fuente, J. M.; Ruiz De Larramendi, I.; Rojo, T.; Liang, X.-J.; et al. The Challenge To Relate the Physicochemical Properties of Colloidal Nanoparticles to Their Cytotoxicity. *Acc. Chem. Res.* **2012**, *46*, 743–749.
70. Xu, L.; Liu, Y.; Chen, Z.; Li, W.; Liu, Y.; Wang, L.; Liu, Y.; Wu, X.; Ji, Y.; Zhao, Y.; et al. Surface-Engineered Gold Nanorods: Promising DNA Vaccine Adjuvant for HIV-1 Treatment. *Nano Lett.* **2012**, *12*, 2003–2012.
71. Li, Y.; Zhou, Y.; Wang, H.-Y.; Perrett, S.; Zhao, Y.; Tang, Z.; Nie, G. Chirality of Glutathione Surface Coating Affects the Cytotoxicity of Quantum Dots. *Angew. Chem., Int. Ed.* **2011**, *50*, 5860–5864.
72. Zhong, Y.; Tian, G.; Gu, Z.; Yang, Y.; Gu, L.; Zhao, Y.; Ma, Y.; Yao, J. Elimination of Photon Quenching by a Transition Layer To Fabricate a Quenching-Shield Sandwich Structure for 800 nm Excited Upconversion Luminescence of Nd^{3+}-Sensitized Nanoparticles. *Adv. Mater.* **2014**, *26*, 2831–2837.
73. Tian, G.; Yin, W.; Jin, J.; Zhang, X.; Xing, G.; Li, S.; Gu, Z.; Zhao, Y. Engineered Design of Theranostic Upconversion Nanoparticles for Tri-Modal Upconversion Luminescence/Magnetic Resonance/X-ray Computed Tomography Imaging and Targeted Delivery of Combined Anticancer Drugs. *J. Mater. Chem. B* **2014**, *2*, 1379–1389.